Journal of Materials Chemistry A

PAPER

View Article Online
View Journal | View Issue

Cite this: J. Mater. Chem. A, 2016, 4, 11046

Production of $Ni(OH)_2$ nanosheets by liquid phase exfoliation: from optical properties to electrochemical applications†

Andrew Harvey,‡[ab] Xiaoyun He,‡[ab] Ian J. Godwin,[ab] Claudia Backes,[ab] David McAteer,[ab] Nina C. Berner,[ac] Niall McEvoy,[ac] Auren Ferguson,[ab] Aleksey Shmeliov,[ac] Michael E. G. Lyons,[ac] Valeria Nicolosi,[ac] Georg S. Duesberg,[ac] John F. Donegan[ab] and Jonathan N. Coleman*[ab]

Received 5th April 2016
Accepted 20th June 2016

DOI: 10.1039/c6ta02811j

www.rsc.org/MaterialsA

Here we demonstrate that liquid phase exfoliation can be used to convert layered crystals of nickel hydroxide into $Ni(OH)_2$ nanosheets in relatively large quantities and without the need for ion intercalation. While other procedures require harsh synthesis conditions and multiple reaction steps, this method involves ultrasonication of commercially available powders in aqueous surfactant solutions and so is relatively mild and potentially scalable. Such mild exfoliation is possible because the surface energy of $Ni(OH)_2$, as measured by inverse gas chromatography, is relatively low at ~70 mJ m^{-2}, similar to other layered materials. TEM, AFM, XPS and Raman spectroscopy show the exfoliated nanosheets to be relatively thin (mean ~10 monolayers thick) and of good quality. Size selection by liquid cascade centrifugation allowed the production of samples with mean nanosheet lengths ranging from 55 to 195 nm. Optical measurements on dispersions showed the optical absorption coefficient spectra to be relatively invariant with nanosheet size while the scattering coefficient spectra varied strongly with size. The resultant size-dependence allows the extinction spectra to be used to estimate nanosheet size as well as concentration. We used the exfoliated nanosheets to prepare thin film electrodes for use in supercapacitors and as oxygen evolution catalysts. While the resultant capacitance was reasonably high at ~1200 F cm^{-3} (20 mV s^{-1}), the catalytic performance was exceptional with currents of 10 mA cm^{-2} observed at overpotentials as low as 297 mV, close to the state of the art.

1. Introduction

Over the last few years, 2-dimensional (2D) materials have become a very important part of nano-materials science.[1,2] A wide range of such materials have been studied, from the prototypical graphene to a host of inorganic 2D materials including BN;[3] transition metal dichalcogenides (TMDs, *e.g.* MoS_2 and WSe_2);[1] transition metal oxides (TMOs, *e.g.* MnO_2 and MoO_3);[4] III–VIs such as InSe[5] and elemental 2D materials such as phosphorene,[6] silicone,[7] stanene[8] and most recently[9] atomically thin 2D boron. These materials are very exciting, not only because they display interesting properties, but because of their potential for use in applications.[2] Here, their diversity is a strength: the many different types[10] of 2D materials leads to a very broad palette of properties and potential uses. As a result, 2D materials have been demonstrated in applications as diverse as electronic devices,[2] water filters[11] and drug delivery.[12]

Two-dimensional materials are produced by a variety of methods including mechanical cleavage,[13,14] synthesis,[15,16] growth[17,18] and various liquid exfoliation techniques,[19–21] with each method having advantages and disadvantages. For many applications,[10] sample preparation requires access to liquid dispersions of 2D nanosheets. Such nanosheets are 2D platelets which have thicknesses of ~nm, but lateral dimensions of ~μm. Their availability in liquids facilitates their processing into useful structures such as composites or thin films.[10] A number of liquid exfoliation methods exist including:[10] oxidation (*e.g.* oxidative exfoliation of graphite to give graphene oxide),[22] exfoliation by ion intercalation (*e.g.* exfoliation of MoS_2 by lithium intercalation)[21] and exfoliation by ion exchange (*e.g.* exfoliation of layered oxides or double hydroxides by weakening the interlayer interaction *via* exchange of existing interlayer ions by bulkier substitutes).[23] Such methods give largely monolayer nanosheets in reasonable quantities but suffer from the disadvantage that all involve multistep chemical processes.

Recently, an alternative approach,[19,24] called liquid phase exfoliation (LPE),[25] has been developed to exfoliate uncharged

[a]CRANN & AMBER, Trinity College Dublin, Dublin 2, Ireland. E-mail: colemaj@tcd.ie
[b]School of Physics, Trinity College Dublin, Dublin 2, Ireland
[c]School of Chemistry, Trinity College Dublin, Dublin 2, Ireland

† Electronic supplementary information (ESI) available. See DOI: 10.1039/c6ta02811j

‡ These authors contributed equally.

layered crystals (*i.e.* those without interlayer ions) to give liquid-dispersed nanosheets. This method involves the production of few-layer nanosheets by shearing[26] or ultrasonication[20] of layered crystals in appropriate stabilising liquids (*i.e.* certain solvents[27] and surfactant[28] or polymer solutions[29]). In each case, interactions between the stabilising liquid and the nanosheet surface reduce the net exfoliation energy and stabilise the nanosheets against aggregation.[24] The resultant dispersions are quite stable and can be produced at concentrations[30] exceeding 1 g L^{-1}. It should be noted that this method produces mostly few-layer nanosheets (typically ~1–10 stacked monolayers), with monolayer contents which are low compared to the methods described above. Nevertheless, LPE has been applied to a wide range of 2D materials including graphene,[19,31,32] BN,[3] TMDs,[20,33] TMOs,[34,35] GaS,[36] phosphorene[37,38] and MXenes.[39] This method has a very important advantage that it is simple and potentially scalable and cheap.[26,40] The resultant dispersions can very easily be processed into nanostructured materials by a range of methods such as spray casting,[41] inkjet printing,[42,43] gravure printing[44] and freeze drying.[45] These structures have been used in a wide range of applications from barrier composites[46,47] to battery electrodes[48] to photodetectors.[49,50]

Because the variety of 2D materials is such an advantage, it will be important to continually increase the number of families of 2D materials that can be exfoliated. The ability to exfoliate new families of 2D materials will undoubtedly expand the number of potential applications of the materials class as a whole. One family of 2D materials that has been exfoliated by chemical means but not by facile methods such as LPE is the layered double hydroxides (LDHs).[23,51,52] The LDHs are a family of layered compounds with monolayers having the general chemical formula of

$$[M_{1-x}^{2+}M_x^{3+}(OH)_2]^{x+}[A_{x/n}^{n-}]^{x-}\cdot mH_2O \quad (1)$$

where A^{n-} represent charge balancing anions which tend to reside between the layers and M^{2+} and M^{3+} are divalent and trivalent metal ions ($M^{2+} = Mg^{2+}$, Fe^{2+}, Co^{2+}, Ni^{2+} *etc.* and $M^{3+} = Fe^{3+}$, Al^{3+}, Co^{3+} *etc.*). Monolayers consist of a central layer of metal ions sandwiched between layers of –OH groups. In general these materials differ from the more well-known 2D materials such as MoS_2 in that the monolayers tend to be charged and accompanied by the charge balancing anions described above. LDH crystals can be exfoliated down to monolayers by methods involving ion exchange (the reader is referred to a number of excellent reviews by Sasaki *et al.* on this topic).[23,51] Such methods typically involve exchanging the charge balancing interlayer anions with more bulky ions such as dodecyl sulphate, resulting in weakening of the interlayer interaction.[51] The resultant swelled crystals can then be exfoliated in solvents such as formamide[51,53] and water.[54] However such chemical exfoliation methods tend to involve multiple steps and be considerably less straightforward than LPE.

However, a subset of LDHs are considerably less complex than implied above. In eqn (1), if $x = 0$, the structure becomes $[M(OH)_2]$, where the basal plane is not charged, and no charge balancing counter-ions are necessary. The most well-known materials of this type are $Ni(OH)_2$, $Co(OH)_2$ and $Mg(OH)_2$, all of which have layered structures. While nanosheets of these materials have been produced by chemical synthesis methods,[55–61] relatively few papers describe their production by exfoliation of layered crystals. Those papers that do describe exfoliation of $Ni(OH)_2$ require specially synthesised starting material containing intercalated surfactant.[62,63] Such experiments involve lengthy multistep synthetic methods incorporating hydrolysis reactions, airtight conditions and heating of the suspension for several days before the final product is formed. Compared to such methods, we believe LPE has many advantages, not least that it is quick, cheap, scalable and doesn't require the use of dangerous chemicals or solvents.

In fact, such a facile method of producing LDH nanosheets would be extremely welcome from an applications perspective. For example, LDH nanosheets such as $Ni(OH)_2$ and $Co(OH)_2$ have shown significant potential for use in electrochemical applications. Both materials have been demonstrated as high-capacity electrode materials for supercapacitors[61] and high-performance electrocatalysts for the oxygen evolution reaction (OER).[57,60,64–67] In application such as these, LPE nanosheets may display a distinct advantage. Previous work has shown that by controlling the dimensions[68] of liquid exfoliated WS_2 nanosheets, the performance of supercapacitor electrodes and hydrogen evolution catalytic electrodes could be maximised.[69] Furthermore, LPE nanosheet dispersions can be formed into films with easily controlled thickness or mixed with carbon nanotubes to form composites, allowing further enhancements of catalytic activity[70] or capacitance.[71] Thus, liquid exfoliation of LDH nanosheets should facilitate the maximisation of their applications potential.

Here, we will focus on $Ni(OH)_2$ as a representative example of an uncharged layered double hydroxide (for structure see Fig. 1A, inset). We show that $Ni(OH)_2$ nanosheets can be produced by liquid phase exfoliation in both the organic solvent *N*-methyl-pyrrolidone or in water using the surfactant sodium cholate as a stabiliser. Raman and XPS spectroscopy were used to confirm the nanosheets to be $Ni(OH)_2$ while liquid cascade centrifugation was used to produce size-selected fractions.[68] We characterise the dependence of the optical properties of the dispersions on nanosheet size, leading to metrics which allow the estimation of not only nanosheet concentration but also lateral size from extinction spectra. Finally we show that films of these nanosheets can be used to prepare high performance supercapacitor electrodes and oxygen evolution electrocatalysts.

2. Results and discussion

2.1 Starting material

Layered $Ni(OH)_2$ was purchased in powder form from Sigma Aldrich (cost 27 c/g). In our experience, such powders often contain non-negligible quantities of impurity material, the presence of which can negatively affect the exfoliation procedure. In an attempt to remove some of these impurities, we employed a pre-treatment procedure which involved sonicating 3 g of powder for 2 hours in 80 mL water followed by a centrifugation step (1 h at 4.5 krpm, 2150*g*) to separate the solubilised

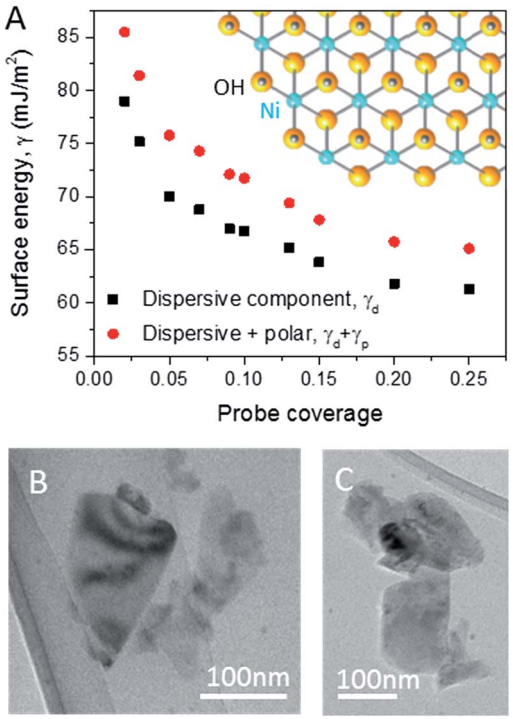

Fig. 1 (A) Measurement of surface energy of $Ni(OH)_2$ layered powder as a function of probe coverage. Data is given for both the dispersive component, δ_d, and the total surface energy (dispersive + polar, δ_d + δ_p). Inset: structure of nickel hydroxide, $Ni(OH)_2$. Blue, Ni; yellow, O; silver, H. (B and C) TEM images of $Ni(OH)_2$ nanosheets produced by exfoliation in the solvent *N*-methyl-pyrrolidone (surface energy $\sim$ 70 mJ m^{-2}).

and unstable components. Here the sediment contained the treated $Ni(OH)_2$ crystallites while the supernatant is expected to contain any impurity material. The sediment was then dried to give a pre-treated powder. We note that, in addition to removing water-soluble impurities, such a procedure generally improves the yield of any subsequent exfoliation process.[72]

Both starting material and pre-treated powder were analysed by XRD (Fig. S1†) to determine their structure.[73] The XRD patterns of both bulk and pre-treated $Ni(OH)_2$ were consistent with single phase[74] β-$Ni(OH)_2$ with the expected crystalline hexagonal structure (a = 0.3126 nm, c = 0.4605 nm).[75] As no peaks from other phases were found, this suggests the layered material to consist of only one phase and contain only single valence Ni^{2+}.[76] This is important as the absence of the charge-balancing counter-ions which are often found in LDHs would be expected to make LPE much more straightforward. In addition, XPS (Fig. S2†) confirms the material to be relatively pure containing no other nickel species than Ni^{2+}.

2.2 Surface energy and solvent exfoliation

Since 2008 it has been known that layered crystals can be exfoliated in solvents so long as the surface energy of the solvent matches that of the layered crystal[19,20,24] (N.B. the surface energy of a liquid is typically $\sim$29 mJ m^{-2} higher than its surface tension due to the contribution of surface entropy).[77] For example MoS_2 and $MoSe_2$ both have surface energies of $\sim$75 mJ m^{-2} (as measured by inverse gas chromatography) and can both be well-exfoliated in solvents such as *N*-methyl-pyrrolidone which have surface energy in the vicinity of 70 mJ m^{-2}.[27] Thus, in order to assess the feasibility of liquid phase exfoliation of $Ni(OH)_2$, it is important to know it's approximate surface energy.

To this end, we used inverse gas chromatography to analyse $Ni(OH)_2$ layered powder, measuring the dispersive component of the surface energy and estimating the contribution due to polar interactions. Inverse gas chromatography (IGC) is a well-established method for measuring the surface energy of heterogeneous solids.[78–80] IGC is a gas sorption technique that operates by injecting different kinds of probe solvents into a column containing the sample and measuring the time taken for them to elute through it. The elution time can then be used to measure the sample's surface energy. By using alkane probes, the dispersive surface energy, γ_d,[81–83] can be measured while polar probes can be used to estimate the polar component of the surface energy, γ_p.[84,85] The total surface energy (γ_T) is generally taken as the sum of these components.[86] Modern IGC equipment measures surface energy profiles, which map the surface energy of a sample as a function of surface coverage of the probe molecule, by carefully controlling the amount of probe injected into the column.[86,87] This is important because low coverage measurements tend to probe high binding energy sites which are generally associated with defects (here most probably flake edges). Only at higher coverage is the intrinsic surface energy measured. We will assume that these high-coverage, intrinsic surface energies are associated with the basal plane of $Ni(OH)_2$. A detailed description of the measurements is given in the ESI.†

We measured the surface energy of $Ni(OH)_2$ layered powder using alkane probes to measure the dispersive component of the surface energy and a combination of dichloromethane and ethyl acetate to measure the polar component. Shown in Fig. 1A are data for both γ_d and the total surface energy, $\gamma_T = \gamma_d + \gamma_p$, both plotted *versus* probe coverage (see ESI† for details). Both curves saturate at probe coverage of >0.2, giving a basal plane dispersive, polar and total surface energies of γ_d = 61 mJ m^{-2}, γ_p = 4 mJ m^{-2} and so γ_T = 65 mJ m^{-2}. We note that the polar component (and so the total surface energy) is somewhat dependent of the exact probe used. As such, we used a complementary technique to measure the specific free energy of absorption of dichloromethane, ethyl acetate, 1-propanol, ethanol and methanol onto $Ni(OH)_2$ (see ESI†). We found these absorption free energies of the alcohols to be 1.8–2.2 times higher than those for dichloromethane and ethyl acetate. This suggests that the polar component of the surface energy may actually be higher than the values given by the basic surface energy measurement with probably values in the range 4–9 mJ m^{-2}. This implies the total surface energy to lie in the range γ_T = 65–70 mJ m^{-2}.

This surface energy value is reasonably close to values of $\sim$75 mJ m^{-2}, recently measured for MoS_2 and $MoSe_2$.[27] This implies that it should be possible to exfoliate $Ni(OH)_2$ in *N*-methyl-pyrrolidone, a solvent commonly used to exfoliate layered

compounds.[25] To test this, we sonicated ($t = 4$ h) pre-treated $Ni(OH)_2$ in *N*-methyl-pyrrolidone (powder concentration $C_i = 20$ g L^{-1}) in a metal beaker (volume, $V = 80$ mL) using an ultrasonic tip (see Methods for details). In order to remove any unexfoliated material, the dispersion was then centrifuged ($t_{cf} =$ 120 min at 1.5 krpm, 240*g*), resulting in a milky green liquid. The contents of this liquid were then analysed using TEM. Large quantities of 2D nanosheets were observed with example images shown in Fig. 1B and C. By filtration and weighing, we measured the dispersed concentration to be ~0.5 mg mL^{-1}.

While these results clearly show that $Ni(OH)_2$ can be exfoliated in *N*-methyl-pyrrolidone, solvent exfoliation has some disadvantages, with typical examples being high solvent boiling point and toxicity. As a result, it is becoming much more common to exfoliate layered materials by sonication in water-surfactant solutions.[28] Usually, any layered material that can be exfoliated in solvents can also be exfoliated in water-surfactant solutions. In addition, surfactant exfoliation often results in nanosheets which are thinner than those found by solvent exfoliation.[68] Because of these reasons we will now focus on liquid phase exfoliation of $Ni(OH)_2$ in water-surfactant solutions.

2.3 Liquid phase exfoliation using surfactants

In order to demonstrate surfactant exfoliation of $Ni(OH)_2$ nanosheets, pre-treated $Ni(OH)_2$ powder (powder concentration $C_i = 20$ g L^{-1}) was added to water and sodium cholate ($C_{SC} =$ 9 g L^{-1}) and sonicated ($t = 4$ h) in a metal beaker (volume, $V =$ 80 mL) using an ultrasonic tip (see Methods for details and ESI† for information about other surfactants). The dispersion was then centrifuged ($t_{cf} = 120$ min at 1.5 krpm, 240*g*) to remove unexfoliated material. This set of conditions results in a stable dispersion with a pale green colour which we refer to as the standard sample (Fig. 2A, inset). To confirm exfoliation, transmission electron microscopy (TEM) was performed on the dispersion by dropping a few drops of dispersion onto a holey carbon grid. TEM images show the dispersion to contain large quantities of well-exfoliated, electron-transparent nanosheets with well-defined edges (Fig. 2A and S4†). Statistical analysis shows the nanosheets in the standard sample to be quite small, as shown by the histogram in Fig. 2B. The mean nanosheet lateral size (*i.e.* the length, defined as the maximum dimension) was $\langle L \rangle = 126 \pm 4$ nm. We also performed atomic force microscopy (AFM) on a standard sample which had been deposited on a Si/SiO_2 surface with a typical image shown in the inset of Fig. 2C. The lateral nanosheet size (represented by the length, *L*) varied in the range 20–200 nm, in reasonable agreement with TEM data. Larger flakes tended to be thicker with $L \approx 10N$, where *N* is the number of monolayers per nanosheet (Fig. 2C). The nanosheet thickness (Fig. 2D), was in the range $1 \leq N \leq 30$, and followed a lognormal distribution, as previously observed for liquid exfoliated BN and WS_2.[68,88] The mean thickness was $\langle N \rangle = 10.6 \pm 0.4$, similar to the value found for liquid exfoliated black phosphorous nanosheets.[89] Although only ~1% of the nanosheets have been identified as monolayer $Ni(OH)_2$, we note that 28% of the nanosheets had $N \leq 6$ layers.

We note that liquid phase exfoliation is quite simple compared to the ion-exchange-based exfoliation methods often used from LDHs.[23,51] During the procedure, the ultrasonication step breaks up the crystallites,[88] producing large quantities of nanosheets.[72] For surfactant exfoliation, these nanosheets are rapidly (within ms)[90,91] coated with sodium cholate surfactant molecules. The combination of bound negatively charged cholate groups and the diffuse cloud of Na^+ ions results in the formation of a non-zero electric potential in the vicinity of the nanosheet surface, the so-called zeta potential.[92] As a result, adjacent nanosheets feel an electrostatic repulsive force which stabilises them against aggregation.

It is important to assess the mass of nanosheets produced by this exfoliation method. While this is usually achieved by measuring concentration using optical spectroscopy *via* the absorption coefficient, this is not completely straightforward for exfoliated nanosheets. This is because the measured optical extinction, Ext (defined *via* $T = 10^{-Ext}$), contains contributions from both absorption and scattering,[68,93] with the size-dependence of the scattering component making concentration measurements unreliable. To address this, we measured the extinction spectrum of the standard sample which was converted into the extinction coefficient (ε) spectrum following careful measurements (see Methods) of the dispersed nanosheet mass (using $Ext = \varepsilon Cl$, where *C* and *l* are concentration and cell length). We then used an integrating sphere to separate the absorption and scattering components,[93] to obtain absorption (α) and scattering (σ) coefficient spectra (where $\varepsilon(\lambda) = \sigma(\lambda) + \alpha(\lambda)$). All three spectra are plotted in Fig. 2E. It is clear that the extinction spectrum is dominated by scattering with the absorption being very weak in comparison. The absorption coefficient spectrum (Fig. 2E, inset) displays a band edge at ~300 nm (~4.1 eV) as well as absorption peaks associated with the Ni^{2+} ions at 386 nm and 654 nm. We note that the optical spectra will be discussed in more detail in a subsequent section of this manuscript.

As described below, the optical absorption coefficient at 386 nm was measured to be $\langle \alpha_{386\ nm} \rangle = 14$ L g^{-1} m^{-1}. This value can be used to measure the nanosheet concentration from the absorbance (Abs) *via* $Abs_{386\ nm} = \alpha_{386} Cl$. Alternatively, as we demonstrate below, a careful analysis of the extinction spectrum can be used to obtain the concentration. We used the optical spectra to estimate the nanosheet concentration for a range of exfoliation parameters. In these experiments the centrifugation rate was kept at 1.5 krpm (240*g*, 2 h) and the supernatants analysed. We prepared nanosheet dispersions for a range of different surfactant concentrations ($C_i = 10$ g L^{-1}, $t_{sonic} = 1$ h, $V = 50$ L) with the resultant concentrations plotted in Fig. 2F *vs.* C_{surf}. As observed previously by Varrla *et al.* and Zhao *et al.* we see a peak at ~9 g L^{-1}, which is reasonably close to the critical micelle concentration (CMC) of sodium cholate (~6 g L^{-1}) as expected.[94,95] The zeta potential (ζ) showed a steady increase with C_{surf} (Fig. 2G), indicating a steady increase in surfactant coverage on the nanosheet surface. We also varied the sonication time ($C_i = 20$ g L^{-1}, $C_{surf} = 9$ g L^{-1}, $V = 80$ mL) and the concentration of $Ni(OH)_2$ powder, C_i ($C_{surf} = 9$ g L^{-1}, $t_{sonic} = 1$ h, $V = 50$ mL) with the measured nanosheet

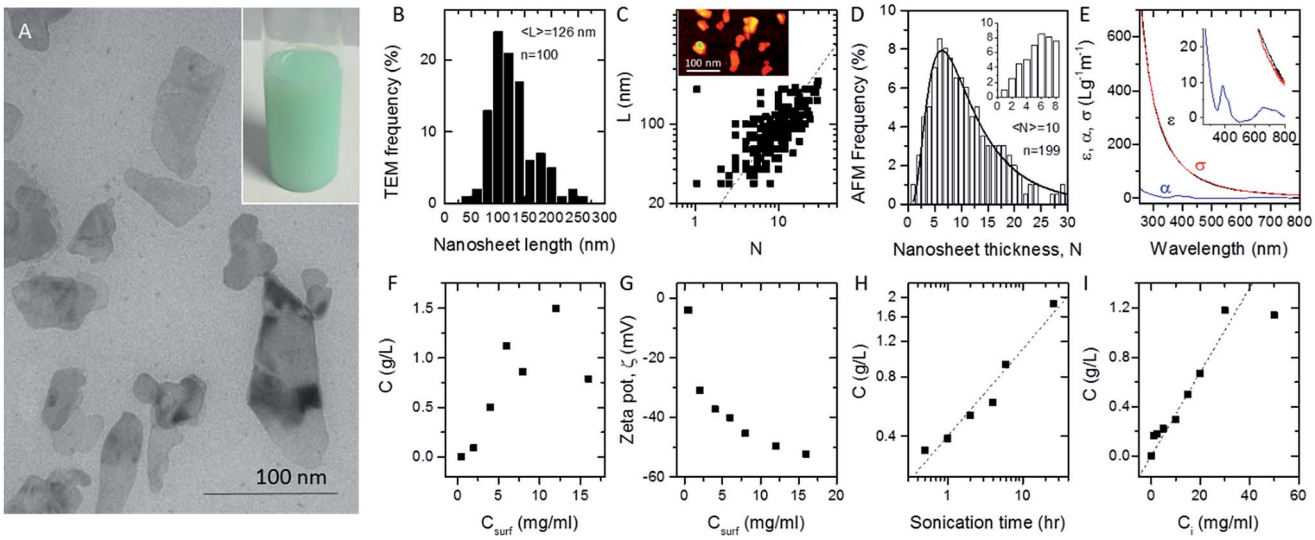

Fig. 2 (A) Representative low resolution TEM image of $Ni(OH)_2$ nanosheets. Inset: photograph of typical $Ni(OH)_2$ dispersion in surfactant solution (H_2O + sodium cholate) showing distinctive green colour. (B) Histogram showing flake length distribution of a standard $Ni(OH)_2$ dispersion (C_i = 20 g L^{-1}, C_{surf} = 9 g L^{-1}, t_{sonic} = 4 h, f = 1.5 krpm, t_{cf} = 120 min). (C) AFM data for nanosheet length plotted *versus* nanosheet thickness for a standard $Ni(OH)_2$ dispersion. The dashed line represents $L = 10N$. Inset: sample AFM image. (D) Histogram of nanosheet thicknesses, N, as measured by AFM. The line represents a log-normal distribution. Inset: magnified image of low N portion of histogram. (E) Optical extinction, absorption, and scattering spectra of $Ni(OH)_2$ in surfactant solution. Inset: magnified view showing absorption spectrum. (F) Final $Ni(OH)_2$ nanosheet concentration plotted against surfactant concentration showing a peak at ~10 g L^{-1} of sodium cholate. The dispersions in 1F were prepared with initial powder concentration C_i = 10 g L^{-1}, t_{sonic} = 1 h and were centrifuged at f = 1.5 krpm for 120 min. (G) Zeta potential plotted against surfactant concentration of dispersions from 1F. (H) Final concentration of $Ni(OH)_2$ plotted against sonication time indicating a square root dependence (dashed line). The dispersions in 1H were prepared with C_i = 20 g L^{-1}, surfactant concentration C_{surf} = 9 g L^{-1} and were centrifuged at f = 1.5 krpm for 120 min. (I) Final concentration of $Ni(OH)_2$ nanosheets plotted *vs.* initial bulk $Ni(OH)_2$ concentration. The dispersions in 1I were prepared with C_{surf} = 9 g L^{-1}, t_{sonic} = 1 h and were centrifuged at f = 1.5 krpm for 120 min.

concentration shown in Fig. 2H and I and the related extinction spectra shown in ESI Fig. S3.† We found the concentration to scale as the square root of sonication time, as is generally found for LPE,[30,34,36] and linearly with C_i, as expected.[28,36] We note that we achieved concentrations as high as 2–3 g L^{-1} and production rates as large as 1–2 mg min^{-1}. These concentrations and production rates are relatively high for LPE nanosheet dispersions produced by sonication and compare well to typical values of ~2 g L^{-1} and 0.25 mg min^{-1} for graphene[26,94] and >1 g L^{-1} and 0.1 mg min^{-1} for MoS_2.[96,97]

2.4 Characterisation of $Ni(OH)_2$ nanosheets

Once the $Ni(OH)_2$ nanosheets were dispersed in the liquid phase, it was possible to perform more detailed characterisation. To achieve this, we prepared thin films by vacuum filtration onto nitrocellulose membranes. Scanning electron microscopy (SEM, Fig. 3A) imaging showed these films to consist of disordered arrays of nanosheets and appear structurally similar to films of other nanosheets types produced by LPE.[28,34,36,98,99] Raman spectroscopy (λ = 532 nm) was used to examine both the pre-treated powder and the nanosheet film, with averaged spectra shown in Fig. 3B (and Fig. S5†). Both spectra show three distinct main peaks at 324, 458 and 3583 cm^{-1} which correspond to E_g and A_{1g} Raman-active transitions characteristic for β-$Ni(OH)_2$.[100] No spectral changes are observed going from powder to nanosheets implying that no physical damage occurs during the exfoliation process. This is further supported by IR spectra (ESI Fig. S6†). A more detailed discussion on the vibrational modes is presented in the ESI.†

X-ray photo-electron spectroscopy (XPS) is an extremely powerful tool to monitor surface chemistry and chemical compositions. Shown in Fig. 3C–F are Ni 2p and O 1s XPS core level spectra measured on both the pre-treated powder (C and D), and exfoliated $Ni(OH)_2$ nanosheets (E and F). The complex metal core level spectra of the Ni 2p core-level were fitted using the parameters established by Biesinger *et al.*[101] Fitting revealed both the pre-treated sample and exfoliated samples to consist almost exclusively of $Ni(OH)_2$. Although this data does not allow us to accurately distinguish between α, β and γ $Ni(OH)_2$, we can conclude that the samples contain virtually no NiO or NiOOH and <1% Ni metal. The corresponding O 1s core-level spectra mainly show the expected $Ni(OH)_2$ contribution at ~531 eV (grey). There is also a broad component on the high binding energy shoulder (purple), which contributes ~30% for the pre-treated sample and ~23% for the nanosheets. We attribute this to a combination of organic impurities remaining in the pre-treated sample and sodium cholate in the exfoliated sample, as well as residual nitrate from the synthesis as observed by Raman and IR spectroscopy (Fig. S5 and S6†). We note that sonication during the exfoliation process did not result in an increased NiO_x content as shown by the Ni 2p and O 1s core level spectra of the pre-treated and processed $Ni(OH)_2$ (Fig. 3C and D).

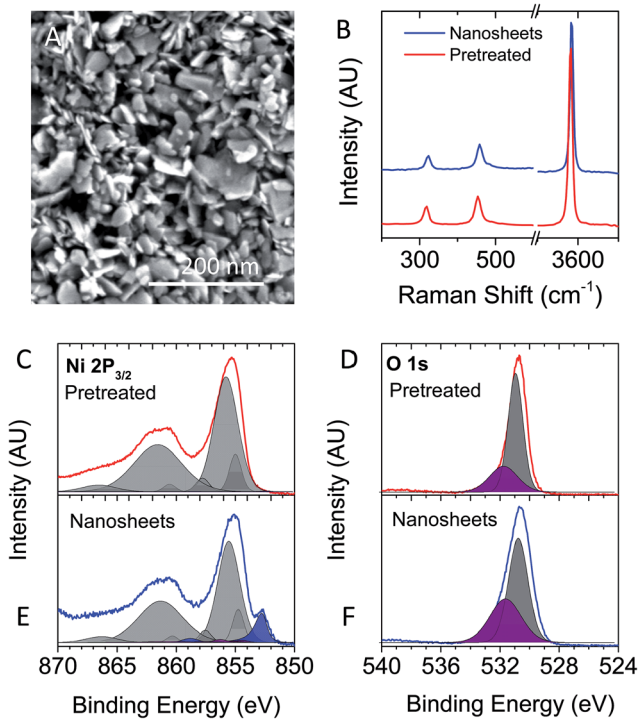

Fig. 3 (A) Representative SEM image of a film made with the filtered standard dispersion (H_2O + sodium cholate, C_i = 20 g L^{-1}, C_{surf} = 9 g L^{-1}, t_{sonic} = 4 h, f = 1.5 krpm, t_{cf} = 120 min). The scale corresponds to 200 nm. (B) Raman spectrum (excitation wavelength = 532 nm, mean of 20 spectra) of standard film and pre-treated powder showing characteristic phonons of the $Ni(OH)_2$. (C–F) Fitted XPS core level spectra of pre-treated powder (C and D) and a film of reaggregated, exfoliated nanosheets (E and F). (C and E) Ni $2P_{3/2}$ core level spectra. (D and F) O 1s core level spectra.

2.5 Size selection and optical characterisation of $Ni(OH)_2$ nanosheets

One significant advantage of dispersions produced by LPE is that they can be readily size-selected. There are a number of ways in which as-produced nanosheet dispersions can be separated into fractions containing different sized nanosheets.[102–107] Here we used liquid cascade centrifugation[68] (LCC), a method that involves a number of sequential centrifugation steps, to isolate nanosheets in different size ranges (see Methods and ref. 68). One advantage of this method is the ease with which high concentration, size-selected dispersions can be achieved. Here we produced five size-selected dispersions which we labelled in order of decreasing size: XL, L, M, S and XS.

In each case, the dispersions were analysed using TEM as described earlier, with sample images shown in the insets of Fig. 4A and B for the XL and XS samples. We performed statistical analysis of the nanosheet lengths with histograms shown in Fig. 4A and B, again for the XL and XS samples. Additional histograms and images are shown in the ESI (Fig. S8†). The mean nanosheet lengths ranged from 55 nm to 195 nm for the XS and XL samples respectively as shown in the lower inset of Fig. 4B.

It has previously been reported that nanosheets size has a number of distinct effects on the optical properties of nanosheet dispersions.[68,93] As a result, we measured the extinction, scattering and absorbance coefficient spectra for the five size-selected dispersions as shown in Fig. 4C–E. It is clear from this data that the extinction coefficients (Fig. 4C) are very sensitive to nanosheet size with ε increasing strongly with $\langle L \rangle$ at all wavelengths. In addition, as indicated previously, the scattering spectra (Fig. 4D) appear very similar to the extinction spectra for all nanosheet sizes confirming the optical properties to be dominated by scattering. The absorption spectra are shown in Fig. 4E and are virtually independent of length in both shape and magnitude. The peaks at 386 nm and 654 nm did not shift with nanosheet size. This is expected as these absorption transitions are associated with the Ni^{2+} ions which have a characteristic length scale much smaller than the size of the nanosheets.[108] The peaks at 700 nm and 400 nm are due to the $^3A_2 \rightarrow {}^3T_1(^3F)$ and $^3A_2 \rightarrow {}^3T_1(^3P)$ transitions respectively (there is also a peak at ~1100 nm which is due to the $^3A_2 \rightarrow {}^3T_2(^3F)$ transition, see ESI, Fig. S7†). These transitions are all associated with Ni^{2+} in an octahedral symmetry and are assigned on the basis of the d^8 system with the local crystal field altering the free ion levels. More detailed analysis is given in the ESI.†

The extinction coefficient at 386 nm, $\varepsilon_{386\ nm}$, is plotted *versus* $\langle L \rangle$ in Fig. 4F. This parameter is almost identical to the scattering coefficient due to the very small value of the absorption coefficient at this wavelength. The extinction coefficient increases strongly with nanosheet length in a manner which can be described empirically by

$$\varepsilon_{386\ nm} \cong \sigma_{386\ nm} = 0.035\langle L \rangle^2 \quad (2)$$

(where $\langle L \rangle$ is in nm). This behaviour is essentially a manifestation of the length dependence of the scattering coefficient. While such behaviour could, in principle, be described by Mie theory,[109] the complexity involved is considerable. We know of no theoretical studies which predict the size dependence of the scattering coefficient of ensembles of nanoscale discs and would allow validation of eqn (2).

The scattering spectra in Fig. 4D are characterised by a power law decay, $\sigma \propto \lambda^{-n}$, which holds in the entire non-resonant regime (*i.e.* λ > 300 nm). Such behaviour has been observed previously for 2D materials such as BN, MoS_2 and WS_2,[20,93] and is consistent with Mie scattering.[110] The scattering exponent, n, can be extracted from either the extinction or scattering spectra and is plotted *versus* $\langle L \rangle$ in Fig. 4G. This graph shows n to be very close to 4 for very small nanosheets but to fall rapidly as the nanosheet length increases. This is not unexpected. For very small objects, with $L \ll \lambda$, we would expect light to be scattered primarily *via* Rayleigh scattering which is characterised by a scattering exponent of $n = 4$. For larger nanosheets, Mie scattering becomes predominant, resulting in a reduction in n (ref. 36 and 89). We can use a purely empirical relationship to fit this data, finding

$$n = 4[1 + (\langle L \rangle/257)^{-2.5}] \quad (3a)$$

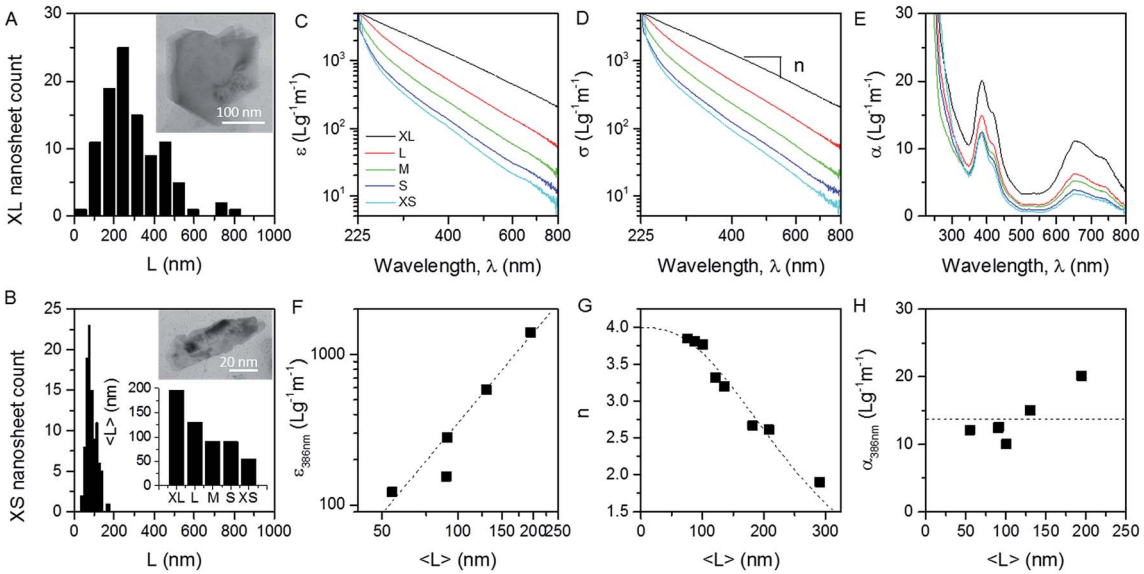

Fig. 4 Dependence of dispersion optical properties on nanosheet size. (A and B) Histograms showing nanosheet length distributions for XL and XS $Ni(OH)_2$ nanosheets. Inset: representative TEM images. (B) Lower inset: mean length of size-selected nanosheets. (C–E) Extinction, scattering and absorption coefficients for XL, L, M, S, XS sizes of $Ni(OH)_2$ nanosheets respectively. The dispersions in (Fig. 3C–E) were prepared using C_i = 20 g L^{-1}, C_{surf} = 9 g L^{-1} and t_{sonic} = 4 h. (F) Extinction coefficients (λ = 387 nm) as a function of $\langle L \rangle$. The fit line in Fig. 3F can be used to determine the extinction coefficient for a dispersion with a known mean nanosheet length. (G) Long wavelength scattering exponent, n, measured from scattering (or extinction) spectra, plotted *versus* TEM $\langle L \rangle$, for size-selected $Ni(OH)_2$ in surfactant solution. (H) Absorption coefficients (λ = 387 nm) as a function of $\langle L \rangle$. The dashed line shows the mean value of 14 L g^{-1} m^{-1}.

where $\langle L \rangle$ is in nm. This expression is quite useful as it allows the mean nanosheet length to be found by estimating n from the scattering, or more practically from the extinction spectrum using

$$\langle L \rangle = 257[(4/n) - 1]^{0.4} \quad (3b)$$

Shown in Fig. 4H is the absorption coefficient at 386 nm, $\alpha_{386\ nm}$, plotted *versus* $\langle L \rangle$. Although $\alpha_{386\ nm}$ appears to increase with $\langle L \rangle$, this is most likely due to scatter associated with the errors due to calculating α from the difference between two large and similar numbers (ε and σ). Thus, we expect $\alpha_{386\ nm}$ to be independent of $\langle L \rangle$ and be controlled by the number of Ni^{2+} ions per volume. Calculating a mean value gives $\langle \alpha_{386\ nm} \rangle$ = 14 L g^{-1} m^{-1}. We can use this to find the optical cross section of the Ni^{2+} ions to be $s = 2.2 \times 10^{-24}$ m^2 (s is defined *via* $T = 10^{-sNl}$, where N is the number of Ni^{2+} ions per unit volume). This can be compared to data in ref. 111 for Ni^{2+} ions in MgF_2 from which we can estimate a Ni^{2+} cross section of $s = 1.6 \times 10^{-24}$ m^2, which is very close to the value obtained here (N.B. we estimated s from ref. 111 using $T = e^{-2.303sNl}$, in order to maintain consistency between their parameter definition and ours). Although this value of $\alpha_{386\ nm}$ can be used to calculate the $Ni(OH)_2$ nanosheet concentration from the absorbance as mentioned above, this is not very practical as an integrating sphere is required to extract the absorbance from the extinction. In practice, it is much more straightforward to combine the empirical relationships described by eqn (2) and (3a) to give another empirical expression

$$\varepsilon_{386\ nm} = 2312\left[\frac{4}{n} - 1\right]^{0.8} \quad (4)$$

where $\varepsilon_{386\ nm}$ is in L g^{-1} m^{-1}. Then, once n is extracted from the extinction spectrum (*e.g.* using $\sigma \cong \varepsilon \propto \lambda^{-n}$ in the wavelength range 300–800 nm), eqn (4) can be used to find $\varepsilon_{386\ nm}$, which in turn can be used to find the concentration from the extinction *via* $Ext_{386\ nm} = \varepsilon_{386\ nm} Cl$. Essentially, this means that the nanosheet concentration can be found by extracting $Ext_{386\ nm}$ and n from an extinction spectrum and using:

$$C = \frac{Ext_{386\ nm}}{2312l}\left[\frac{4}{n} - 1\right]^{-0.8} \quad (5)$$

where l is the cell length in meters and C is in g L^{-1}.

2.6 Electrochemical applications of $Ni(OH)_2$ nanosheets: supercapacitor electrodes and oxygen evolution reaction catalysts

Layered $Ni(OH)_2$ has previously been demonstrated to have significant potential for electrochemical applications in areas such as supercapacitor electrodes,[112,113] as a catalyst for the oxygen evolution reaction,[114,115] and as a cathode material in batteries.[116,117] In the past, standard synthetic methods[76,115,118] have yielded layered crystallites rather than a truly 2-dimensional nanomaterial. More recently, attention has focused on identifying preparation methods which give nanostructured forms of $Ni(OH)_2$ in order to enhance both charge storage capacity[32] and catalytic activity.[53] The most common high surface area forms are nanoparticles/spheres and 2-dimensional nanosheets. Such nanostructured forms of $Ni(OH)_2$ would be expected to be preferred for electrochemical applications due to their high surface area and increased number of accessible catalytically active sites. In fact supercapacitor

electrodes prepared from $Ni(OH)_2$ nanospheres[112] and nanosheets[113] have demonstrated stable capacitance of >2000 F g^{-1}, significantly larger than found for most nanostructured materials. Similarly oxygen evolution catalysts[119] prepared from nanostructured $Ni(OH)_2$ nanoparticles[115] and nanosheets[53] showed improved performance with benchmark currents of 10 mA cm^{-2} at overpotentials as low as 300 mV. Such high activities have been attributed to the high density of active edge sites. In addition, it has been shown that the presence of iron in such nanostructures can result in significant improvements in OER performance.[120]

However, synthesis of nanostructured $Ni(OH)_2$, often involves harsh synthesis conditions using high voltages and lengthy procedures.[112,121] As described above, chemical exfoliation of $Ni(OH)_2$ is also rather complex.[63] A number of authors have pointed out that a facile and low-cost method of producing high-quality $Ni(OH)_2$ nanosheets is urgently required.[113] We believe that liquid phase exfoliation offers a comparatively mild alternative which is scalable in comparison to chemical exfoliation. Below, we will demonstrate the performance of LPE nanosheets in electrochemical applications.

Here we prepared electrodes of $Ni(OH)_2$ nanosheets by spraying the standard dispersion onto commercial Ni foam at a loading level of 0.6 mg cm^{-2} (thickness ~ 3 μm). Ni foam was used here due to its desirable open 3-D structure which allows efficient diffusion of the electrolyte to the catalyst.[122]

Shown in Fig. 5A is an SEM image of the electrode surface immediately after deposition. The electrode consists of a disordered array of nanosheets similar to the filtered film shown in Fig. 3A. Electrodes for use in a number of applications including as OER anodes are often activated by electrochemical pretreatment or activation to obtain a reproducible electrochemical response or to increase the active surface area by surface roughening.[115,123] This can be achieved either by repeatedly cycling the potential between fixed limits or by application of a constant potential or current.[124] Here we activated our nickel hydroxide electrode by applying a constant current density of 10 mA cm^{-2} for 100 hours. Shown in Fig. 5B is an SEM image of a $Ni(OH)_2$ nanosheet electrode after activation with both morphology and surface coverage appearing unchanged, indicating good mechanical stability with minimal physical spalling of the film. High resolution TEM studies (see ESI†) suggested the hexagonal structure of the as-prepared nanosheets to become amorphous after activation. We suggest this reflects the transformation of the β-$Ni(OH)_2$ sample into β-Ni(OOH) and/or γ-Ni(OOH). The resultant loss of crystallinity is consistent with the results of Sac-Epée and co-workers.[125]

2.6.1 Supercapacitor electrodes. For energy storage applications, $Ni(OH)_2$ has found wide use due to the large pseudocapacitance associated with the main redox reaction:

$$Ni(OH)_2 + OH^- \rightarrow Ni(OOH) + H_2O + e^- \quad (6)$$

Here, we explored this by testing these films as supercapacitor electrodes. As noted above, the charge storage capability of $Ni(OH)_2$ is largely due to main Ni(II/III) redox reaction, which is clearly visible in Fig. 5C, and can be described by eqn (6). We found the capacitance (dV/dt = 40 mV s^{-1}) of the as-deposited film to be significantly larger than that of the Ni foam, with activation resulting in a significant further increase. This activation-induced increase in charge under the main Ni(II/III) redox peak suggests an increase in redox activity. This is consistent with the suggestion that activation results in the transformation of $Ni(OH)_2$ to NiOOH, with the higher oxidation

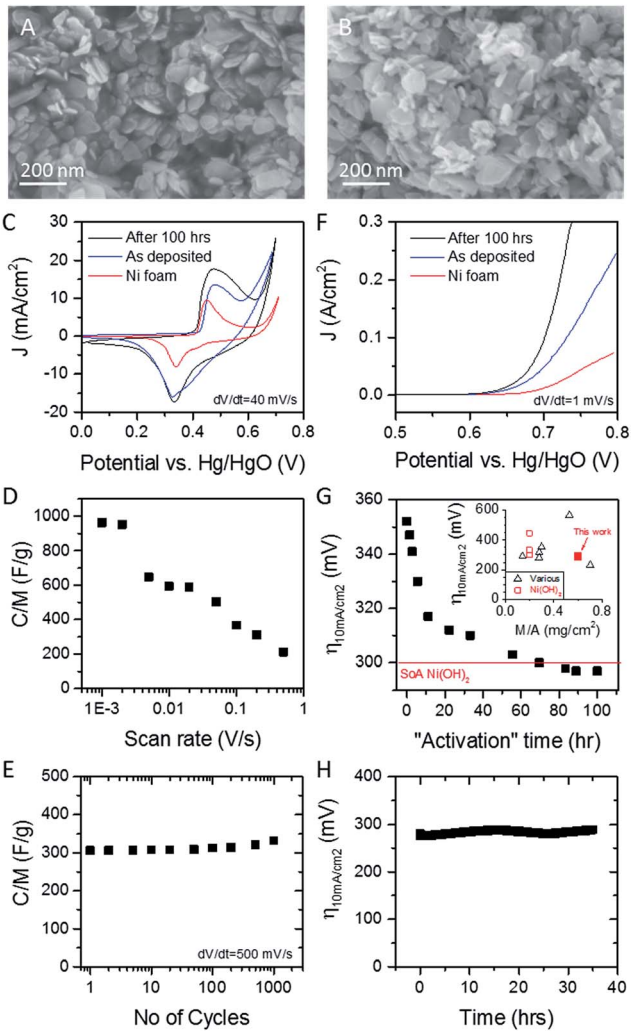

Fig. 5 Applications potential of liquid exfoliated $Ni(OH)_2$ nanosheets. (A and B) SEM images of an as-prepared $Ni(OH)_2$ film and (B) a film after activation by 100 h polarisation with current density of 10 mA cm^{-2}. (C) Cyclic voltammograms measured for supercapacitor electrodes fabricated from $Ni(OH)_2$ films on Ni foam current collectors before and after activation. A CV curve measured for the bare Ni foam is shown for comparison. (D) Specific capacitance (normalised to $Ni(OH)_2$ mass) plotted as a function of scan rate. (E) Stability behaviour for an already activated film showing capacitance plotted *versus* cycle number (0.7 mg cm^{-2}, scan range −160 mV to 400 mV, dV/dt = 500 mV s^{-1}). (F) Polarisation curves for OER from $Ni(OH)_2$ electrodes fabricated from $Ni(OH)_2$ films on Ni foam current collectors before and after activation with the equivalent curve for the bare Ni foam shown for comparison. (G) Overpotential required to produce J = 10 mA cm^{-2}, $\eta_{10\ mA\ cm^{-2}}$, plotted as a function of activation time. Inset: comparison with literature values. (H) Stability behaviour for an already activated film showing $\eta_{10\ mA\ cm^{-2}}$ plotted as a function of time (0.7 mg cm^{-2}, *iR* corrected).

state resulting in an increase in redox charge storage. However, we note that the increase could partially be explained by removal of residual surfactant during the activation process.

As shown in Fig. 5D, the capacitance decreases with increasing scan rate as expected due to either diffusion[126] or charge transport[127] limitations. The measured capacitance value of 600 F g^{-1} at 20 mV s^{-1} is comparable to other nickel hydroxide materials reported in the literature and agrees with data measured by charge/discharge (see ESI†). Li and co-workers[112] prepared $Ni(OH)_2$ with a capacitance of 1250 F g^{-1} at 20 mV s^{-1}, albeit prepared using a more complicated electrodeposition method. In addition, Yan and co-workers[128] prepared $Ni(OH)_2$ and $Ni(OH)_2$/graphene composite, using a microwave assisted synthesis, and obtained a capacitance value of 420 F g^{-1} and 800 F g^{-1} respectively at 20 mV s^{-1}. It is worth noting that these values are much larger than those typically found for graphene-based supercapacitors (typically ~200 F g^{-1}).[129] When expressed on a volumetric basis, the capacitance at 20 mV s^{-1} was ~1200 F cm^{-3}, considerably higher than the value of ~500 F cm^{-3}, reported recently for electrodes of 1T-MoS_2.[130]

We tested the stability of an already activated (100 h polarisation) electrode by repeatedly measuring CV curves over many cycles (scan range −160 mV to 400 mV, $dV/dt = 500$ mV s^{-1}). As shown in Fig. 5E, the specific capacity was invariant with cycle number showing very good stability.

2.6.2 Oxygen evolution reaction catalysts. Perhaps more interesting is the possibility of using these nanosheets to produce electrocatalysts for the oxygen evolution reaction. Such a reaction occurs at the anode of water electrolysers to generate oxygen *via*

$$4OH^- \rightarrow O_2 + 2H_2O + 4e^- \quad (7)$$

and requires an appropriate catalyst.[131] As mentioned above, $Ni(OH)_2$ has been extensively used in this role. However, it is worth noting that, although the literature generally refers to $Ni(OH)_2$ as an effective catalyst for the OER, it is actually NiOOH which is believed to be responsible for catalysis. While NiOOH may have been formed from $Ni(OH)_2$ during activation, it is also known to form[114] upon application of a significantly anodic potential just prior to the OER, as described by eqn (6). However, for the sake of simplicity, we will continue to use the term $Ni(OH)_2$ when referring to our catalyst. Using the electrodes described above, we performed linear sweeps in 1 M NaOH for the bare nickel foam, an as-produced electrode and an electrode after 100 h of activation at 10 mA cm^{-2}, with the polarisation curves shown in Fig. 5F (impedance curves are given in the ESI†). It is clear that the as-produced film is a much better catalyst than the bare Ni foam with activation resulting in a further increase in current density at a given potential by a factor of ×2.5. The Tafel slope was close to 60 mV dec^{-1}, both before and after activation, indicating that the activation process does not affect the rate limiting step of the reaction. The overpotential required to achieve a current density of 10 mA cm^{-2} is plotted *versus* activation time in Fig. 5G and shows a steady decreases with activation time, reaching 297 mV for long times.

Similar behavior upon activation of a nickel electrode has been seen elsewhere in the literature. For example, Mellsop and co-workers[132] found that a hydrous nickel oxide electrode, activated by polarization at 50 mA cm^{-2} in 6 M KOH, showed the overpotential required to generate 50 mA cm^{-2} of current to decrease by 200 mV over 7 h of activation. However, they were unable to explain the exact origin of this improved activity. As mentioned above, we suggest activation to involve the conversion of $Ni(OH)_2$ to a more catalytically active phase of NiOOH.[119]

We tested the stability of an already activated (100 h polarisation) electrode by measuring $\eta_{10\ mA\ cm^{-2}}$ as a function of time. As shown in Fig. 5H, $\eta_{10\ mA\ cm^{-2}}$ was invariant with time showing very good stability. One point to be stressed here is that usually OER catalysts lose activity with polarisation time either through physical spalling or dissolution of the film.

We can compare these results to the literature for a range of OER catalysts by plotting the overpotential required to achieve a current density of 10 mA cm^{-2} ($\eta_{10\ mA\ cm^{-2}}$), which is a common benchmark used in the literature,[133] *versus* the electrode mass loading.[64–67,134,135] We find our material to display values of $\eta_{10\ mA\ cm^{-2}}$ which are superior to all other values for pure $Ni(OH)_2$ nanosheets and, indeed, approaching the global state of the art of OER catalysts as shown in Fig. 5G (inset). We believe this to be an important result. The nanosheet catalytic electrodes produced in this work have not been optimised in any way. Neither the nanosheet size[69] nor the electrode thickness[70] have been varied to maximise the number of active catalytic sites. Nor have we added nano-conductors such as carbon nanotubes or graphene to improve the catalytic performance.[70,136] We believe that once future work is carried out to fully optimise the performance of LPE $Ni(OH)_2$ nanosheets, it will be possible to prepare catalytic electrodes which perform significantly beyond the start of the art.

3. Conclusions

In conclusion, we have demonstrated that liquid phase exfoliation can be used to exfoliate layered $Ni(OH)_2$ crystals from commercially available powder to give liquid dispersions of few-layer $Ni(OH)_2$ nanosheets with the identity of the dispersed material being confirmed by SEM, Raman and XPS. This process yields nanosheets in a broad size range at reasonably high concentrations and with production rates which compare well to graphene production by LPE. This process allows the nanosheets to be size-selected in a simple an efficient manner. We found the optical extinction of the dispersions to vary strongly with nanosheet size. Detailed studies showed the nanosheet absorbance to be roughly size invariant but the optical scattering spectra to depend strongly on nanosheet length. LPE results in nanosheet dispersions which are solution-processable and can be easily formed into structures such as films. Here we spray-cast films of $Ni(OH)_2$ nanosheets onto a nickel mesh. However our deposition method could also be applied to any support geometry or material. We demonstrated the utility of these structures *via* electrochemical measurements. We found these films to be extremely effective electrocatalysts for the oxygen evolution reaction and to perform well

as supercapacitor electrodes. Not only were the films shown to be very stable for the OER over a period of several days, with no deactivation of the film occurring, but the catalytic activity was found to increase with use. When comparing to the literature, our $Ni(OH)_2$ films were amongst the most active in the literature for the overpotential required to generate 10 mA cm^{-2} of current (a benchmark commonly used when comparing OER catalysts) as low as 297 mV.

This work has extended LPE to a new class of materials, the layered hydroxides, and further demonstrates the versatility of this method. We view $Ni(OH)_2$ as a model system which we have used to demonstrate LPE. We believe that this work will allow LPE to be used to exfoliate other systems such as $Co(OH)_2$ and $Mg(OH)_2$. Such materials will prove useful in a range of applications from electrochemistry to the development of flame retardant materials.

4. Methods

4.1 Materials

Nickel hydroxide powder (>95% item no. 283662) and sodium cholate (SC, item no. C1254) were purchased from Sigma Aldrich. De-ionized water was prepared in house and all solvents used were purchased with the highest available purity.

4.2 Preparation of $Ni(OH)_2$ nanosheets

Nickel hydroxide powder was pre-treated by sonication using a sonic tip in de-ionized water for 2 h. The dispersion was then centrifuged at 4.5 krpm (2150*g*) for 1 h and the supernatant decanted with the sediment being retained and dried at 60 °C. Pre-treated $Ni(OH)_2$ was sonicated in surfactant and de-ionized water solution using a sonic tip. The sonication was performed using a solid flat head tip (Sonics VX-750) at 60% amplitude with a 6 s on 2 s off pulse rate in an 80 mL metal cup. Mostly ice cooling was used except for the sonication time study, in this instance water cooling was used where a chiller pumps water around the metal cup maintaining a temperature of 15 °C. Once sonicated, the dispersion was centrifuged in a Hettich Mikro 220R centrifuge with a fixed-angle rotor 1060 (N.B.: for this centrifuge, rpm are related to *g*-force *via* RCF = $106.4f^2$, where f is the rotation rate in krpm). The top 60% was then taken from the centrifuged (supernatant) for analysis and the sediment was discarded.

4.3 Optimization of dispersion parameters

The surfactant concentration study entailed sonicating 10 g L^{-1} $Ni(OH)_2$ in 50 mL 1 g L^{-1}, 2 g L^{-1}, 4 g L^{-1}, 6 g L^{-1}, 8 g L^{-1}, 10 g L^{-1}, and 12 g L^{-1} of SC and de-ionized water for 1 h 20 min and centrifuging for 120 min at 1.5 krpm (240*g*) with the supernatant being decanted and analysed. The initial $Ni(OH)_2$ concentration experiments comprised of sonicating 0.1 g L^{-1}, 2.5 g L^{-1}, 5 g L^{-1}, 10 g L^{-1}, 20 g L^{-1}, 50 g L^{-1}, and 75 g L^{-1} $Ni(OH)_2$ powder in 9 g L^{-1} of surfactant solution for 1 h 20 min and centrifuging for 120 min at 1.5 krpm (240*g*) with the supernatant being decanted. The sonication time study was carried out using water cooling, as overnight sonicating was required. 20 g L^{-1} of $Ni(OH)_2$ powder was sonicated in 9 g L^{-1} SC surfactant solution for 24 h with 4 s on 4 s off and 60% amplitude and centrifuging for 120 min at 1.5 krpm (240*g*) with the supernatant being decanted. For all parts, the supernatant was decanted and the absorption and extinction were measured in a 4 mm path length cuvette using a PerkinElmer Lambda 650 spectrometer (see below). The final optimized exfoliation was performed as follows: 20 g L^{-1} of $Ni(OH)_2$ were sonicated for 4 h in 9 g L^{-1} of SC and then centrifuged for 120 min at 1.5 krpm (240*g*).

4.4 Size selection

We used liquid cascade centrifugation with subsequently increasing rotation speeds as previously reported.[68] 20 g L^{-1} $Ni(OH)_2$ in 80 mL of 9 g L^{-1} SC was sonicated for 4 h with a 6 s on 2 s off pulse rate. The 80 mL of sonicated dispersion was centrifuged at 0.5 krpm (27*g*) for 60 min. The sediment was discarded and the supernatant was centrifuged at 1 krpm (100*g*) for 60 min. The sediment after this centrifugation step was redispersed in fresh surfactant solution (C_{SC} = 9 g L^{-1}, 25 mL) in by 5 min bath sonication producing the largest size. The supernatant after the 1 krpm centrifugation step was centrifuged at 1.5 krpm (240*g*) for 60 min, producing the second largest size in the redispersed sediment. These steps were repeated in further increments of 2 krpm (425*g*), 2.5 krpm (665*g*), and 3 krpm (950*g*), thus producing five sizes.

4.5 Characterization and equipment

Optical extinction and absorbance was measured on a PerkinElmer 650 spectrometer in quartz cuvettes with a path length of 0.4 cm. To distinguish between contributions from scattering and absorbance to the extinction spectra, dispersions were measured in an integrating sphere using a home-built sample holder to place the cuvette in the centre of the sphere (N.B. cuvettes need to be transparent to all sides and correct/reproducible positioning is important). The absorbance spectrum is obtained from the measurement inside the sphere. A second measurement on each dispersion was performed outside the sphere in the standard configuration to obtain the extinction spectrum. This allows calculation of the scattering spectrum (extinction minus absorbance).

Low-resolution bright field transmission electron microscopy imaging was performed using a JEOL 2100, operated at 200 kV. Holey carbon grids (400 mesh) were purchased from Agar Scientific and prepared by diluting a dispersion to a low concentration and drop casting onto a grid placed on a filter membrane to wick away excess solvent. Statistical analysis was performed of the flake dimensions by measuring the longest axis of the nanosheet and assigning it as "length", L.

Raman spectroscopy was performed using a WITec alpha 300 with 532 nm excitation laser in air under ambient conditions. The Raman emission was collected by an Olympus 100× objective (N.A. = 0.8) and dispersed by 600 lines per mm gratings. The laser energy was kept below 0.2 mW. The mean of 20 spectra is displayed.

XPS spectra were taken using monochromated Al Kα X-rays from an Omicron XM1000 MkII X-ray source and an Omicron EA125 energy analyzer. The analyzer pass energies were 15 eV for the core-level spectra and 100 eV for the survey spectra. An electron Omicron CN10 flood gun was used for charge compensation in both cases and the binding energy scale was referenced to the adventitious carbon 1s core-level at 284.8 eV. After subtraction of a Shirley background, the core-level spectra were fitted with Gaussian–Lorentzian line shapes using the software CasaXPS. Scanning electron microscopy was performed with a Carl Zeiss Ultra SEM operating at 2 kV. Images were acquired using the secondary electron detector.

Atomic force microscopy (AFM) was carried out on a Dimension ICON3 scanning probe microscope (Bruker AXS S.A.S.) in tapping mode in air under ambient conditions using aluminum coated silicon cantilevers (OTESP-R3). A drop of the dispersion (20 μL) was deposited on a pre-heated (150 °C) Si/SiO_2 wafer (1 × 1 cm^2) with an oxide layer of 300 nm. The high concentration dispersion was diluted with water immediately prior to deposition to reduce surfactant concentrations to yield a pale colloidal dispersion. After deposition, the wafer was rinsed with ~5 mL of water and ~5 mL of isopropanol. Typical image sizes were 2 × 2 μm^2 at scan rates of 0.8–1.0 Hz with 512 lines per image. The apparent thickness was converted to number of layers using previously developed step-height analysis[68,93] as shown in the ESI† for the $Ni(OH)_2$ nanosheets.

4.6 Deposition of $Ni(OH)_2$ film

The $Ni(OH)_2$ films were prepared by diluting the 'suspension' by a factor of three in IPA, to aid adhesion, and sprayed onto the nickel foam electrode using a hand held spray gun. After spraying the films were dried under a nitrogen flow to evaporate any excess solvent. The electrodes were weighed on a balance before and after spraying. The loading was 0.6 mg cm^{-2}. The $Ni(OH)_2$ films were activated by applying a constant current density of 10 mA cm^{-2}.

4.7 General cell set up

All electrochemical experiments were conducted in a conventional three electrode cell kept at 25 °C. Prior to each experiment, the nickel foam (1 cm^2 supplied by Novametcorp USA, density 420 g m^{-2}) was sonicated in 3 M HCl for 5 min to remove any surface oxide and sonicated twice in Millipore water (resistivity > 15 MΩ cm^{-1}) for a further 5 min. A platinum rod was employed as the counter electrode and a mercury–mercuric oxide (Hg/HgO) reference electrode with a 1 M NaOH filling solution (CH Instruments, cat. no. CHI 152) was utilised as the reference standard, therefore all voltages are quoted against this reference electrode unless otherwise stated. The equilibrium potential of the cell $Pt/H_2/OH^-/HgO/Hg$ is 0.926 V at 298 K. Since the equilibrium oxygen electrode potential is 1.229 V *vs.* reversible hydrogen electrode (RHE), it follows that the corresponding value is 0.303 V *vs.* Hg/HgO in the same solution. Hence $E_{Hg/HgO} = E_{RHE} - 0.926$ V. It is common practice in the literature on the OER to express potential in terms of the oxygen evolution overpotential, η, when the reference electrode is a Hg/HgO electrode in the same solution as the working anode. The overpotential therefore is related to E_{meas} measured on the Hg/HgO scale as follows: $E = E_{meas} - 0.303$ V (at $T = 298$ K).

Aqueous 1 M NaOH was used as the electrolyte. This solution was prepared from sodium hydroxide pellets (Sigma-Aldrich, minimum 99% purity). The electrochemical measurements were performed on a Gamry model 600 potentiostat/galvanostat. The redox charge capacitance was measured by integrating the area under the Ni(III/II) redox peak and dividing by the voltage window while normalising for the scan rate.

Acknowledgements

This work was primarily funded by Science Foundation Ireland through the PI program (11/PI/1087). The research leading to these results has also received funding from the European Union Seventh Framework Program under grant agreement no. 604391 Graphene Flagship, the European Research Council (SEMANTICS) and the Science Foundation Ireland (SFI) funded centre AMBER (SFI/12/RC/2278).

References

1 M. Chhowalla, H. S. Shin, G. Eda, L.-J. Li, K. P. Loh and H. Zhang, *Nat. Chem.*, 2013, **5**, 263–275.
2 Q. H. Wang, K. Kalantar-Zadeh, A. Kis, J. N. Coleman and M. S. Strano, *Nat. Nanotechnol.*, 2012, **7**, 699–712.
3 C. Y. Zhi, Y. Bando, C. C. Tang, H. Kuwahara and D. Golberg, *Adv. Mater.*, 2009, **21**, 2889–2893.
4 M. Osada and T. Sasaki, *J. Mater. Chem.*, 2009, **19**, 2503–2511.
5 W. Feng, J. B. Wu, X. L. Li, W. Zheng, X. Zhou, K. Xiao, W. W. Cao, B. Yang, J. C. Idrobo, L. Basile, W. Q. Tian, P. H. Tan and P. A. Hu, *J. Mater. Chem. C*, 2015, **3**, 7022–7028.
6 R. A. Doganov, E. C. T. O'Farrell, S. P. Koenig, Y. Yeo, A. Ziletti, A. Carvalho, D. K. Campbell, D. F. Coker, K. Watanabe, T. Taniguchi, A. H. Castro Neto and B. Ozyilmaz, *Nat. Commun.*, 2015, **6**, 6647.
7 L. Tao, E. Cinquanta, D. Chiappe, C. Grazianetti, M. Fanciulli, M. Dubey, A. Molle and D. Akinwande, *Nat. Nanotechnol.*, 2015, **10**, 227–231.
8 F.-f. Zhu, W.-j. Chen, Y. Xu, C.-l. Gao, D.-d. Guan, C.-h. Liu, D. Qian, S.-C. Zhang and J.-f. Jia, *Nat. Mater.*, 2015, **14**, 1020–1025.
9 A. J. Mannix, X.-F. Zhou, B. Kiraly, J. D. Wood, D. Alducin, B. D. Myers, X. Liu, B. L. Fisher, U. Santiago, J. R. Guest, M. J. Yacaman, A. Ponce, A. R. Oganov, M. C. Hersam and N. P. Guisinger, *Science*, 2015, **350**, 1513–1516.
10 V. Nicolosi, M. Chhowalla, M. G. Kanatzidis, M. S. Strano and J. N. Coleman, *Science*, 2013, **340**, 1420–1438.
11 D. Cohen-Tanugi and J. C. Grossman, *Nano Lett.*, 2012, **12**, 3602–3608.
12 R. Tkacz, R. Oldenbourg, S. B. Mehta, M. Miansari, A. Verma and M. Majumder, *Chem. Commun.*, 2014, **50**, 6668–6671.

13 R. F. Frindt, *Phys. Rev.*, 1965, **140**, A536–A575.
14 K. S. Novoselov, D. Jiang, F. Schedin, T. J. Booth, V. V. Khotkevich, S. V. Morozov and A. K. Geim, *Proc. Natl. Acad. Sci. U. S. A.*, 2005, **102**, 10451–10453.
15 H. Matte, A. Gomathi, A. K. Manna, D. J. Late, R. Datta, S. K. Pati and C. N. R. Rao, *Angew. Chem., Int. Ed.*, 2010, **49**, 4059–4062.
16 H. Matte, B. Plowman, R. Datta and C. N. R. Rao, *Dalton Trans.*, 2011, **40**, 10322–10325.
17 Y.-H. Lee, X.-Q. Zhang, W. Zhang, M.-T. Chang, C.-T. Lin, K.-D. Chang, Y.-C. Yu, J. T.-W. Wang, C.-S. Chang, L.-J. Li and T.-W. Lin, *Adv. Mater.*, 2012, **24**, 2320–2325.
18 C. Berger, Z. M. Song, T. B. Li, X. B. Li, A. Y. Ogbazghi, R. Feng, Z. T. Dai, A. N. Marchenkov, E. H. Conrad, P. N. First and W. A. de Heer, *J. Phys. Chem. B*, 2004, **108**, 19912–19916.
19 Y. Hernandez, V. Nicolosi, M. Lotya, F. M. Blighe, Z. Sun, S. De, I. T. McGovern, B. Holland, M. Byrne, Y. K. Gun'ko, J. J. Boland, P. Niraj, G. Duesberg, S. Krishnamurthy, R. Goodhue, J. Hutchison, V. Scardaci, A. C. Ferrari and J. N. Coleman, *Nat. Nanotechnol.*, 2008, **3**, 563–568.
20 J. N. Coleman, M. Lotya, A. O'Neill, S. D. Bergin, P. J. King, U. Khan, K. Young, A. Gaucher, S. De, R. J. Smith, I. V. Shvets, S. K. Arora, G. Stanton, H.-Y. Kim, K. Lee, G. T. Kim, G. S. Duesberg, T. Hallam, J. J. Boland, J. J. Wang, J. F. Donegan, J. C. Grunlan, G. Moriarty, A. Shmeliov, R. J. Nicholls, J. M. Perkins, E. M. Grieveson, K. Theuwissen, D. W. McComb, P. D. Nellist and V. Nicolosi, *Science*, 2011, **331**, 568–571.
21 G. Eda, H. Yamaguchi, D. Voiry, T. Fujita, M. Chen and M. Chhowalla, *Nano Lett.*, 2011, **11**, 5111–5116.
22 D. R. Dreyer, S. Park, C. W. Bielawski and R. S. Ruoff, *Chem. Soc. Rev.*, 2010, **39**, 228–240.
23 R. Z. Ma and T. Sasaki, *Adv. Mater.*, 2010, **22**, 5082–5104.
24 J. N. Coleman, *Acc. Chem. Res.*, 2013, **46**, 14–22.
25 L. Niu, J. N. Coleman, H. Zhang, H. Shin, M. Chhowalla and Z. Zheng, *Small*, 2016, **12**, 272–293.
26 K. R. Paton, E. Varrla, C. Backes, R. J. Smith, U. Khan, A. O'Neill, C. Boland, M. Lotya, O. M. Istrate, P. King, T. Higgins, S. Barwich, P. May, P. Puczkarski, I. Ahmed, M. Moebius, H. Pettersson, E. Long, J. Coelho, S. E. O'Brien, E. K. McGuire, B. M. Sanchez, G. S. Duesberg, N. McEvoy, T. J. Pennycook, C. Downing, A. Crossley, V. Nicolosi and J. N. Coleman, *Nat. Mater.*, 2014, **13**, 624–630.
27 G. Cunningham, M. Lotya, C. S. Cucinotta, S. Sanvito, S. D. Bergin, R. Menzel, M. S. P. Shaffer and J. N. Coleman, *ACS Nano*, 2012, **6**, 3468–3480.
28 R. J. Smith, P. J. King, M. Lotya, C. Wirtz, U. Khan, S. De, A. O'Neill, G. S. Duesberg, J. C. Grunlan, G. Moriarty, J. Chen, J. Z. Wang, A. I. Minett, V. Nicolosi and J. N. Coleman, *Adv. Mater.*, 2011, **23**, 3944–3948.
29 P. May, U. Khan, J. M. Hughes and J. N. Coleman, *J. Phys. Chem. C*, 2012, **116**, 11393–11400.
30 U. Khan, H. Porwal, A. O'Neill, K. Nawaz, P. May and J. N. Coleman, *Langmuir*, 2011, **27**, 9077–9082.
31 L. H. Liu, G. Zorn, D. G. Castner, R. Solanki, M. M. Lerner and M. D. Yan, *J. Mater. Chem.*, 2010, **20**, 5041–5046.
32 W. C. Du, J. Lu, P. P. Sun, Y. Y. Zhu and X. Q. Jiang, *Chem. Phys. Lett.*, 2013, **568**, 198–201.
33 G. S. Bang, K. W. Nam, J. Y. Kim, J. Shin, J. W. Choi and S. Y. Choi, *ACS Appl. Mater. Interfaces*, 2014, **6**, 7084–7089.
34 D. Hanlon, C. Backes, T. M. Higgins, M. Hughes, A. O'Neill, P. King, N. McEvoy, G. S. Duesberg, B. M. Sanchez, H. Pettersson, V. Nicolosi and J. N. Coleman, *Chem. Mater.*, 2014, **26**, 1751–1763.
35 M. M. Y. A. Alsaif, S. Balendhran, M. R. Field, K. Latham, W. Wlodarski, J. Z. Ou and K. Kalantar-Zadeh, *Sens. Actuators, B*, 2014, **192**, 196–204.
36 A. Harvey, C. Backes, Z. Gholamvand, D. Hanlon, D. McAteer, H. C. Nerl, E. McGuire, A. Seral-Ascaso, Q. M. Ramasse, N. McEvoy, S. Winters, N. C. Berner, D. McCloskey, J. F. Donegan, G. S. Duesberg, V. Nicolosi and J. N. Coleman, *Chem. Mater.*, 2015, **27**, 3483–3493.
37 J. Kang, J. D. Wood, S. A. Wells, J.-H. Lee, X. Liu, K.-S. Chen and M. C. Hersam, *ACS Nano*, 2015, **9**, 3596–3604.
38 P. Yasaei, B. Kumar, T. Foroozan, C. Wang, M. Asadi, D. Tuschel, J. E. Indacochea, R. F. Klie and A. Salehi-Khojin, *Adv. Mater.*, 2015, **27**, 1887–1892.
39 M. Naguib, O. Mashtalir, J. Carle, V. Presser, J. Lu, L. Hultman, Y. Gogotsi and M. W. Barsoum, *ACS Nano*, 2012, **6**, 1322–1331.
40 M. Yi and Z. Shen, *Carbon*, 2014, **78**, 622–626.
41 B. Mendoza-Sanchez, J. Coelho, A. Pokle and V. Nicolosi, *Electrochim. Acta*, 2015, **174**, 696–705.
42 D. J. Finn, M. Lotya, G. Cunningham, R. J. Smith, D. McCloskey, J. F. Donegan and J. N. Coleman, *J. Mater. Chem. C*, 2014, **2**, 925–932.
43 F. Torrisi, T. Hasan, W. P. Wu, Z. P. Sun, A. Lombardo, T. S. Kulmala, G. W. Hsieh, S. J. Jung, F. Bonaccorso, P. J. Paul, D. P. Chu and A. C. Ferrari, *ACS Nano*, 2012, **6**, 2992–3006.
44 E. B. Secor, S. Lim, H. Zhang, C. D. Frisbie, L. F. Francis and M. C. Hersam, *Adv. Mater.*, 2014, **26**, 4533–4538.
45 X. T. Zhang, Z. Y. Sui, B. Xu, S. F. Yue, Y. J. Luo, W. C. Zhan and B. Liu, *J. Mater. Chem.*, 2011, **21**, 6494–6497.
46 J. Biscarat, M. Bechelany, C. Pochat-Bohatier and P. Miele, *Nanoscale*, 2015, **7**, 613–618.
47 S. Xie, O. M. Istrate, P. May, S. Barwich, A. P. Bell, U. Khana and J. N. Coleman, *Nanoscale*, 2015, **7**, 4443–4450.
48 J. Sun, H.-W. Lee, M. Pasta, H. Yuan, G. Zheng, Y. Sun, Y. Li and Y. Cui, *Nat. Nanotechnol.*, 2015, **10**, 980–985.
49 G. Cunningham, D. Hanlon, N. McEvoy, G. S. Duesberg and J. N. Coleman, *Nanoscale*, 2015, **7**, 198–208.
50 F. Withers, H. Yang, L. Britnell, A. P. Rooney, E. Lewis, A. Felten, C. R. Woods, V. Sanchez Romaguera, T. Georgiou, A. Eckmann, Y. J. Kim, S. G. Yeates, S. J. Haigh, A. K. Geim, K. S. Novoselov and C. Casiraghi, *Nano Lett.*, 2014, **14**, 3987–3992.
51 R. Z. Ma, Z. P. Liu, L. Li, N. Iyi and T. Sasaki, *J. Mater. Chem.*, 2006, **16**, 3809–3813.
52 G. Abellán, C. Martí-Gastaldo, A. Ribera and E. Coronado, *Acc. Chem. Res.*, 2015, **48**, 1601–1611.

53 F. Song and X. Hu, *Nat. Commun.*, 2014, **5**, 4477.
54 T. Hibino and M. Kobayashi, *J. Mater. Chem.*, 2005, **15**, 653–656.
55 G. H. Li, X. W. Wang, H. Y. Ding and T. Zhang, *RSC Adv.*, 2012, **2**, 13018–13023.
56 H. T. Cui, J. Y. Xue, W. Z. Ren and M. M. Wang, *J. Nanopart. Res.*, 2014, **16**, 2601.
57 Y. Zhu, C. Cao, S. Tao, W. Chu, Z. Wu and Y. Li, *Sci. Rep.*, 2014, 5787.
58 G. Li, X. Wang, H. Ding and T. Zhang, *RSC Adv.*, 2012, **2**, 13018–13023.
59 J. X. H. Cui, W. Ren and M. Wang, *J. Nanopart. Res.*, 2014, **16**, 2181.
60 S. Jiang, Z. Gui, G. Chen, D. Liang and J. Alam, *ACS Appl. Mater. Interfaces*, 2015, **7**, 14603–14613.
61 M. Aghazadeh, S. Dalvand and M. Hosseinifard, *Ceram. Int.*, 2014, **40**, 3485–3493.
62 D. Wang, W. Yan and G. G. Botte, *Electrochem. Commun.*, 2011, **13**, 1135–1138.
63 S. Ida, D. Shiga, M. Koinuma and Y. Matsumoto, *J. Am. Chem. Soc.*, 2008, **130**, 14038–14039.
64 L. A. Stern, L. G. Feng, F. Song and X. L. Hu, *Energy Environ. Sci.*, 2015, **8**, 2347–2351.
65 Y. Wang, S. Li, S. Peng, L. Zhang, A. M. Al-Enizi, H. Zhang, X. Sun and G. Zheng, *Adv. Energy Mater.*, 2015, 1501661.
66 H. J. Shi and G. H. Zhao, *J. Phys. Chem. C*, 2014, **118**, 25939–25946.
67 M. Gao, W. Sheng, Z. Zhuang, Q. Fang, S. Gu, J. Jiang and Y. Yan, *J. Am. Chem. Soc.*, 2014, **136**, 7077.
68 C. Backes, B. M. Szydlowska, A. Harvey, S. Yuan, V. Vega-Mayoral, B. R. Davies, P. L. Zhao, D. Hanlon, E. Santos, M. I. Katsnelson, W. J. Blau, C. Gadermaier and J. N. Coleman, *ACS Nano*, 2016, **10**, 1589–1601.
69 Z. Gholamvand, D. McAteer, A. Harvey, C. Backes and J. N. Coleman, *Chem. Mater.*, 2016, **28**, 2641–2651.
70 D. McAteer, Z. Gholamvand, N. McEvoy, A. Harvey, E. O'Malley, G. S. Duesberg and J. N. Coleman, *ACS Nano*, 2016, **10**, 672–683.
71 T. M. Higgins, D. McAteer, J. C. M. Coelho, B. M. Sanchez, Z. Gholamvand, G. Moriarty, N. McEvoy, N. C. Berner, G. S. Duesberg, V. Nicolosi and J. N. Coleman, *ACS Nano*, 2014, **8**, 9567–9579.
72 S. Barwich, U. Khan and J. N. Coleman, *J. Phys. Chem. C*, 2013, **117**, 19212–19218.
73 Q. Wang and D. O'Hare, *Chem. Rev.*, 2012, **112**, 4124–4155.
74 Y. Wang, Q. Zhu and H. Zhang, *Chem. Commun.*, 2005, 5231–5233, DOI: 10.1039/b508807k.
75 Y. Wang, Q. Zhu, L. Tao and X. Su, *J. Mater. Chem.*, 2011, **21**, 9248–9254.
76 D. S. Hall, D. J. Lockwood, C. Bock and B. R. MacDougall, *Proc. R. Soc. A*, 2015, **471**, 20140792.
77 J. Lyklema, *Colloids Surf., A*, 1999, **156**, 413–421.
78 J. Y. Y. H. Pirre, P. Ylä-Mäihäniemi, F. Thielmann and D. R. Williams, *Langmuir*, 2008, **24**, 9551–9557.
79 M. G. Huson, J. S. Church, A. A. Kafi, A. L. Woodhead, J. Khoo, M. S. R. N. Kiran, J. E. Bradby and B. L. Fox, *Carbon*, 2014, **68**, 240–249.
80 R. Menzel, A. Bismarck and M. S. P. Shaffer, *Carbon*, 2012, **50**, 3416–3421.
81 H. Balard, D. Maafa, A. Santini and J. B. Donnet, *J. Chromatogr. A*, 2008, **1198–1199**, 173–180.
82 J. B. Donnet, S. J. Park and M. Brendle, *Carbon*, 1992, **30**, 263–268.
83 E. Papirer, E. Brendle, F. Ozil and H. Balard, *Carbon*, 1999, **37**, 1265–1274.
84 J. Donnet, S. J. Park and H. Balard, *Chromatographia*, 1991, **31**, 434–440.
85 R. Ho, S. J. Hinder, J. F. Watts, S. E. Dilworth, D. R. Williams and J. Y. Heng, *Int. J. Pharm.*, 2010, **387**, 79–86.
86 S. C. Das, I. Larson, D. A. Morton and P. J. Stewart, *Langmuir*, 2011, **27**, 521–523.
87 R. R. Smith, D. R. Williams, D. J. Burnett and J. Y. Y. Heng, *Langmuir*, 2014, **30**, 8029–8035.
88 K. Kouroupis-Agalou, A. Liscio, E. Treossi, L. Ortolani, V. Morandi, N. M. Pugno and V. Palermo, *Nanoscale*, 2014, **6**, 5926–5933.
89 D. Hanlon, C. Backes, E. Doherty, C. S. Cucinotta, N. C. Berner, C. Boland, K. Lee, A. Harvey, P. Lynch, Z. Gholamvand, S. F. Zhang, K. P. Wang, G. Moynihan, A. Pokle, Q. M. Ramasse, N. McEvoy, W. J. Blau, J. Wang, G. Abellan, F. Hauke, A. Hirsch, S. Sanvito, D. D. O'Regan, G. S. Duesberg, V. Nicolosi and J. N. Coleman, *Nat. Commun.*, 2015, **6**, 8563.
90 M. S. Strano, V. C. Moore, M. K. Miller, M. J. Allen, E. H. Haroz, C. Kittrell, R. H. Hauge and R. E. Smalley, *J. Nanosci. Nanotechnol.*, 2003, **3**, 81–86.
91 A. E. Frise, G. Pagès, M. Shtein, I. Pri Bar, O. Regev and I. Furó, *J. Phys. Chem. B*, 2012, **116**, 2635–2642.
92 J. Israelachvili, *Intermolecular and Surface Forces*, Academic Press, 2nd edn, 1991.
93 C. Backes, R. J. Smith, N. McEvoy, N. C. Berner, D. McCloskey, H. C. Nerl, A. O'Neill, P. J. King, T. Higgins, D. Hanlon, N. Scheuschner, J. Maultzsch, L. Houben, G. S. Duesberg, J. F. Donegan, V. Nicolosi and J. N. Coleman, *Nat. Commun.*, 2014, **5**, 4576.
94 E. Varrla, K. R. Paton, C. Backes, A. Harvey, R. J. Smith, J. McCauley and J. N. Coleman, *Nanoscale*, 2014, **6**, 11810–11819.
95 J. Zhao, Z. Wang, Q. Zhao and B. Xing, *Environ. Sci. Technol.*, 2014, **48**, 331–339.
96 E. Varrla, C. Backes, K. R. Paton, A. Harvey, Z. Gholamvand, J. McCauley and J. N. Coleman, *Chem. Mater.*, 2015, **27**, 1129–1139.
97 A. O'Neill, U. Khan and J. N. Coleman, *Chem. Mater.*, 2012, **24**, 2414–2421.
98 S. B. Xie, O. M. Istrate, P. May, S. Barwich, A. P. Bell, U. Khana and J. N. Coleman, *Nanoscale*, 2015, **7**, 4443–4450.
99 M. Lotya, Y. Hernandez, P. J. King, R. J. Smith, V. Nicolosi, L. S. Karlsson, F. M. Blighe, S. De, Z. M. Wang, I. T. McGovern, G. S. Duesberg and J. N. Coleman, *J. Am. Chem. Soc.*, 2009, **131**, 3611–3620.
100 D. S. Hall, D. J. Lockwood, S. Poirier, C. Bock and B. R. MacDougall, *J. Phys. Chem. A*, 2012, **116**, 6771–6784.

101 M. C. Biesinger, B. P. Payne, L. W. M. Lau, A. Gerson and R. S. C. Smart, *Surf. Interface Anal.*, 2009, **41**, 324–332.
102 C. Backes, R. J. Smith, N. McEvoy, N. C. Berner, D. McCloskey, H. C. Nerl, A. O'Neill, P. J. King, T. Higgins, D. Hanlon, N. Scheuschner, J. Maultzsch, L. Houben, G. S. Duesberg, J. F. Donegan, V. Nicolosi and J. N. Coleman, *Nat. Commun.*, 2014, **5**, 4576.
103 C. Backes, B. M. Szydlowska, A. Harvey, S. Yuan, V. Vega-Mayoral, B. R. Davies, P. L. Zhao, D. Hanlon, E. Santos, M. I. Katsnelson, W. J. Blau, C. Gadermaier and J. N. Coleman, *ACS Nano*, 2016, **10**, 1589–1601.
104 A. A. Green and M. C. Hersam, *Nano Lett.*, 2009, **9**, 4031–4036.
105 U. Khan, A. O'Neill, H. Porwal, P. May, K. Nawaz and J. N. Coleman, *Carbon*, 2012, **50**, 470–475.
106 J. Kang, J. W. T. Seo, D. Alducin, A. Ponce, M. J. Yacaman and M. C. Hersam, *Nat. Commun.*, 2014, **5**, 5478.
107 F. Bonaccorso, M. Zerbetto, A. C. Ferrari and V. Amendola, *J. Phys. Chem. C*, 2013, **117**, 13217–13229.
108 Y. J. Qi, H. Y. Qi, J. H. Li and C. J. Lu, *J. Cryst. Growth*, 2008, **310**, 4221–4225.
109 H. C. van de Hulst, *Light Scattering by Small Particles*, Dover Publications, 1981.
110 M. Retsch, M. Schmelzeisen, H. J. Butt and E. L. Thomas, *Nano Lett.*, 2011, **11**, 1389–1394.
111 J. García Solé, L. E. Bausá and D. Jaque, *An Introduction to the Optical Spectroscopy of Inorganic Solids*, Wiley and Sons, 2005.
112 H. B. Li, M. H. Yu, F. X. Wang, P. Liu, Y. Liang, J. Xiao, C. X. Wang, Y. X. Tong and G. W. Yang, *Nat. Commun.*, 2013, **4**, 1894.
113 Y. Zhu, C. Cao, S. Tao, W. Chu, Z. Wu and Y. Li, *Sci. Rep.*, 2014, **4**, 5787.
114 R. L. Doyle, I. J. Godwin, M. P. Brandon and M. E. G. Lyons, *Phys. Chem. Chem. Phys.*, 2013, **15**, 13737–13783.
115 L.-A. Stern and X. Hu, *Faraday Discuss.*, 2014, **176**, 363–379.
116 D. E. Reisner, A. J. Salkind, P. R. Strutt and T. D. Xiao, *J. Power Sources*, 1997, **65**, 231–233.
117 H. Zhang, X. Yu and P. V. Braun, *Nat. Nanotechnol.*, 2011, **6**, 277–281.
118 L. A. Hutton, M. Vidotti, A. N. Patel, M. E. Newton, P. R. Unwin and J. V. Macpherson, *J. Phys. Chem. C*, 2011, **115**, 1649–1658.
119 I. J. Godwin and M. E. G. Lyons, *Electrochem. Commun.*, 2013, **32**, 39–42.
120 L. Trotochaud, S. L. Young, J. K. Ranney and S. W. Boettcher, *J. Am. Chem. Soc.*, 2014, **136**, 6744–6753.
121 M. Gong, Y. Li, H. Wang, Y. Liang, J. Z. Wu, J. Zhou, J. Wang, T. Regier, F. Wei and H. Dai, *J. Am. Chem. Soc.*, 2013, **135**, 8452–8455.
122 C. Guan, J. Liu, C. Cheng, H. Li, X. Li, W. Zhou, H. Zhang and H. J. Fan, *Energy Environ. Sci.*, 2011, **4**, 4496–4499.
123 J. C. Hoogvliet, M. Dijksma, B. Kamp and W. P. van Bennekom, *Anal. Chem.*, 2000, **72**, 2016–2021.
124 L. Trotochaud, J. K. Ranney, K. N. Williams and S. W. Boettcher, *J. Am. Chem. Soc.*, 2012, **134**, 17253–17261.
125 N. Sac-Epée, M. R. Palacìn, A. Delahaye-Vidal, Y. Chabre and J. M. Tarascon, *J. Electrochem. Soc.*, 1998, **145**, 1434–1441.
126 B. E. Conway, *Electrochemical Supercapacitors Scientific Fundamentals and Technological Applications*, Springer, US, 1999.
127 T. M. Higgins and J. N. Coleman, *ACS Appl. Mater. Interfaces*, 2015, **7**, 16495–16506.
128 J. Yan, Z. Fan, W. Sun, G. Ning, T. Wei, Q. Zhang, R. Zhang, L. Zhi and F. Wei, *Adv. Funct. Mater.*, 2012, **22**, 2632–2641.
129 Y. Wang, Z. Shi, Y. Huang, Y. Ma, C. Wang, M. Chen and Y. Chen, *J. Phys. Chem. C*, 2009, **113**, 13103–13107.
130 M. Acerce, D. Voiry and M. Chhowalla, *Nat. Nanotechnol.*, 2015, **10**, 313–318.
131 K. Zeng and D. Zhang, *Prog. Energy Combust. Sci.*, 2010, **36**, 307–326.
132 S. R. Mellsop, A. Gardiner, B. Johannessen and A. T. Marshall, *Electrochim. Acta*, 2015, **168**, 356–364.
133 C. C. L. McCrory, S. Jung, J. C. Peters and T. F. Jaramillo, *J. Am. Chem. Soc.*, 2013, **135**, 16977–16987.
134 N. Han, F. P. Zhao and Y. G. Li, *J. Mater. Chem. A*, 2015, **3**, 16348–16353.
135 Z. Lu, L. Qian, Y. Tian, Y. Li, X. Sun and X. Duan, *Chem. Commun.*, 2015, 52.
136 Y. Li, H. Wang, L. Xie, Y. Liang, G. Hong and H. Dai, *J. Am. Chem. Soc.*, 2011, **133**, 7296–7299.